SCIENCE CHINA
Technological Sciences

•Article•

July 2022 Vol.65 No.7: 1587–1598
https://doi.org/10.1007/s11431-021-1992-1

Phase selection and microstructure evolution within eutectic Ti-Si alloy solidified at containerless state

LUO ZhiCong, CHANG Jian & WANG HaiPeng*

School of Physical Science and Technology, Northwestern Polytechnical University, Xi'an 710072, China

Received October 24, 2021; accepted December 28, 2021; published online May 25, 2022

Phase selection and microstructure evolution of the undercooled eutectic Ti-Si alloy were systematically investigated by the electromagnetic levitation method, and the maximum undercooling achieved was 318 K ($0.2T_E$). The migration of the liquid-solid interface was *in-situ* detected by a high-speed camera system. When the undercooling is smaller than 140 K, the liquid-solid interface is smooth. Once the undercooling arrives at 230 K, the liquid-solid interface is irregular, which reflects the growth transition from the solute control to the combined controls of solute and thermal. The eutectic growth velocity increases as an exponential function of undercooling. The electromagnetic stirring effect makes it difficult to increase undercooling, but plays an important role in accelerating the eutectic reaction velocity at low and moderate undercoolings. Primary dendritic β-Ti phase appears in the solidified alloy from 63 to 176 K undercoolings, and the microstructure is completely composed of eutectic once the undercoolings increase up to 230 K. When the undercoolings exceed 273 K, the microstructure consists of uniformly distributed irregular eutectic. For the drop tube experiments, the microstructures composed of a large amount of dendritic α-Ti phase and eutectic phase are found in a wide range of diameters from 69 to 725 μm. As the decrease of diameter, the solubility of Si in the dendritic α-Ti phase dramatically increases from 6.80% to 10.73%, and the ratio of the area occupied by the dendritic α-Ti on a cross-section of solidified alloy obviously increases from 23.52% to 41.02%, which result from the combined effects of high undercooling and large cooling rate.

phase selection, microstructure evolution, high undercooling, containerless, large cooling rate

Citation: Luo Z C, Chang J, Wang H P. Phase selection and microstructure evolution within eutectic Ti-Si alloy solidified at containerless state. Sci China Tech Sci, 2022, 65: 1587–1598, https://doi.org/10.1007/s11431-021-1992-1

1 Introduction

The phase selection and microstructure evolution are of great importance in the field of materials science [1–5]. After the undercooled melt completes the phase selection, the solid phase starts growth, which finishes before the microstructure formation. For the alloy systems with different properties, the inherent dendrite growth manner may be different [6,7]. By applying the properties of the alloy melt, the alloys with the same composition could produce different growth characteristics [8,9]. For a long time, the LKT/BCT model has achieved positive results in explaining the dendrite growth velocity with undercooling [10–13]. However, there is a large deviation between the calculated value and the experimental value under a high undercooling condition [10,14], which could attribute to the large deviation between the actual experimental conditions and the model, especially when the internal flow of the melts is very large and the external cooling rate is rather large. It is necessary to understand the process of dendrite growth from a new perspective so as to control the final microstructure. A common feature among the various dendrite growth phenomena is that the dendrite growth contains complicated physical reactions and chemical reactions [15,16]. It should be scientifically feasible to explain nucleation and dendrite growth. The prelude of dendrite growth is nucleation, and the nucleation

*Corresponding author (email: hpwang@nwpu.edu.cn)

of the primary phase depends on the phase selection within the alloy melt. The regulation of microstructure is not only inseparable from the processes of nucleation and dendrite growth, but also inseparable from the phase selection. Therefore, the studies of phase selection and dendrite growth process are helpful to deeply understand the microstructure formation, and the microstructure evolution in turn deepens the understanding of the phase selection and dendrite growth.

As is known, the chemical reactions involve the breaking of old bonds and the new bonds formation. The process of forming new bonds is the key to nucleation and dendrite growth. Recent studies have shown that the nucleation proceeds through an iterative and reversible process between ordered and disordered states [17]. According to the chemical reaction mechanism, there will be a transition state in the process of forming the final product. In the transition state, the valence bonds of the molecules need to be rearranged to form the transition state when the reacting molecules are close each other [9,18,19]. The process of nucleation and phase selection can be considered as the process of reacting molecules forming a transition state and crossing the transition state. An in-depth understanding of the transition state is conducive to controlling nucleation, phase selection, dendrite growth and microstructure formation. As such a transition state is unstable and not easy to retain to room temperature under normal conditions, it is possible to retain it under extraordinary conditions, such as high undercooling or large cooling rate condition. Importantly, it is necessary to choose an appropriate alloy system in order to achieve the above research purpose.

The eutectic alloy is sensitive to competitive nucleation, phase selection and microstructure formation, which is conducive to the study of the above-mentioned scientific problems [20,21]. Additionally, high temperature alloys are of great importance in aviation and automotive industries, including the Ti-based alloys, Ni-based alloys and Nb-based alloys, and hence, they are listed as research candidates due to their engineering applications [22–27]. As a typical eutectic alloy, Ti-Si alloy has excellent casting characteristics as well as good oxidation resistance and creep resistance. Therefore, Ti-Si eutectic composition is selected as the research object. Under normal conditions, it is difficult to obtain high undercooling and large cooling rate, because the heterogeneous nucleation produced by contact with the container makes the undercooled liquid phase unable to achieve high undercooling [28]. Therefore, the containerless state was used to create extraordinary conditions of high undercooling and large cooling rate to achieve the rapid solidification of undercooled liquid Ti-Si alloy [14,29].

In this paper, in order to understand how the phase selection and the microstructure formation process of undercooled Ti-Si eutectic melt change with the undercooling and cooling rate, it is necessary to further study the rapid solidification of the highly undercooled Ti-Si alloy melts. Therefore, the solidification of $Ti_{86.33}Si_{13.67}$ eutectic alloy is conducted by using the extraordinary conditions of electromagnetic levitation and drop tube methods. In addition, the dendrite growth kinetics, phase selection and the microstructure formation of the $Ti_{86.33}Si_{13.67}$ eutectic alloy are studied for the purpose of exploring the eutectic growth kinetics, phase constitution and microstructure evolution.

2 Experimental

2.1 Electromagnetic levitation experiment

The eutectic $Ti_{86.33}Si_{13.67}$ master alloys were prepared by melting pure Ti (99.999%) and Si (99.999%) in an arc melting furnace which was pumped to about 1.0×10^{-4} Pa firstly and then backfilled to 1.0×10^{5} Pa. And then, the master alloy samples of about 6 mm diameter were melted and cooled using an electromagnetic levitation technique, which was backfilled with a mixture of high-purity argon and helium gas to 1.0×10^{5} Pa after it was evacuated to 1.0×10^{-4} Pa. The samples were also overheated to about 200 K by the induction heating device and highly undercooled by cooling helium gas to get different undercoolings when the temperature curves were simultaneously measured by a Raytek Marathon MR1SCF infrared pyrometer, which was also calibrated on the basis of the eutectic reaction temperature T_E of the $Ti_{86.33}Si_{13.67}$ alloy. In order to *in-situ* detect the migration process of the liquid-solid interface, a high-speed camera system was conducted to record the recalescence images in 256 × 192 pixels at a frame rate of 10000 frames per second.

2.2 Drop tube experiment

Drop tube experiment can obtain larger cooling rate [30,31] compared with the electromagnetic levitation method. The rapid solidification experiments of the $Ti_{86.33}Si_{13.67}$ alloy were carried out through a 3 m drop tube technique. The alloy sample with a mass of 1 g was placed inside a quartz tube which was fixed on the top of drop tube technique, and quartz tube had an orifice about 0.5 mm in radius at the bottom. The drop tube was evacuated to about 1.0×10^{-4} Pa and then backfilled with the mixed gas of helium gas and argon gas with a ratio of 0.6 to 1.0×10^{5} Pa. The alloy sample was melted to a liquid and overheated to about 200 K by electromagnetic induction heating. And then, the liquid sample alloy was ejected out from orifice and atomized into many tiny droplets by high pressure helium gas. The atomized tiny droplets were rapidly solidified benefiting from the cooling helium gas.

The solidified alloys were polished and then etched with a solution consisted of 1 mL HF + 1 mL HNO_3+ 8 mL H_2O.

The solidified microstructures were analyzed by a Verios G4 scanning electron microscopy (SEM) and an optical microscopy (OM) as well as an Oxford energy dispersive spectrometer (EDS). The corresponding phase constitutions were determined by a Rigaku D/max 2500 X-ray diffractometer (XRD) and a FEI Talos F200X transmission electron microscope (TEM) as well as a double Cs corrector transmission electron microscope (DC-TEM).

3 Results and discussion

3.1 Rapid solidification process

Liquid eutectic $Ti_{86.33}Si_{13.67}$ alloy was undercooled under the electromagnetic levitation condition and the maximum undercooling ΔT obtained was 318 K ($0.2T_E$). In order to *in-situ* monitor the nonequilibrium phase transition process, the typical heating and cooling curves of the electromagnetically levitated alloy were simultaneously measured, as shown in Figure 1. In Figure 1(a), the first exothermic peak represents the phase change of L (liquid phase) to β-Ti phase and the second peak represents the phase change of L to β-Ti + Ti_5Si_3 phases. The third peak which represents the phase change of β-Ti to α-Ti appears on the cooling curves of the samples, and there is an obvious time interval between the first peak and the second peak. However, there is almost no time interval between the exothermic peaks of L to β-Ti phase and L to β-Ti + Ti_5Si_3 phases at the 176 K undercooling, as displayed in Figure 1(b). Only two exothermic peaks which represent the L to β-Ti + Ti_5Si_3 phases and β-Ti to α-Ti respectively are found at the 318 K undercooling, as seen in Figure 1(c). The average cooling rate R_c is calculated by dividing the difference ΔT_h from the maximum temperature of the overheated melt to the eutectic recalescence temperature by the corresponding time difference Δt_s. The average diameter of the sample is D, the average eutectic reaction time and liquid-solid transition velocity is t_E and V, respectively. Therefore, $V = D/t_E$, and $R_c = \Delta T_h/\Delta t_s$. Obviously, R_c calculated from the cooling curves is less than 100 K/s under the electromagnetic levitation conditions. The difference between the three exothermic peaks at low undercoolings and the two exothermic peaks at high undercoolings reflects the change of solidification path. Additionally, the eutectic reaction time reduces from 1.365 to 1.247 s in an undercooling range of 100 K from 75 to 176 K, while that reduces from 1.247 to 0.01684 s from 176 to 318 K undercooling.

To observe the liquid-solid interface during the eutectic reaction, a high-speed camera system was employed to record the growth process, as shown in Figures 2 and 3. The dark area stands for the undercooled liquid phase while the light area denotes the solid phase due to the release of latent heat during solidification. As for ΔT=140 K, the liquid phase begins to nucleate and grow from the lower right corner. The liquid-solid interface is smooth in Figure 2. Multiple areas begin to nucleate and grow with the advance of the initial solid-liquid interface. Multiple solidified areas are connected together to form a larger solid-liquid interface. This larger liquid-solid interface is still smooth which is also convex to the liquid phase. The migration time lasts 0.763 s.

As ΔT =230 K, the liquid phase begins to nucleate and grow from the upper right corner, and the liquid-solid interface is not regular and smooth once the recalescence time exceeds 0.02 s as shown in Figure 3. There are regions leading to the growth of the solid-liquid interface, and this implies that the process of this eutectic reaction is simultaneously controlled by solute diffusion and thermal diffusion at the 230 K undercooling. Compared with the multiple regions which nucleate and growth at the 140 K undercooling, there is only a large nucleation and growth region. The recalescence time reduces from 0.763 to 0.07 s as the undercooling increases from 140 to 230 K, which demonstrates that the high undercooling accelerates the rapid eutectic growth and dominates the growth transition from solute control to thermal control. Additionally, when the time is before 20 ms and after 48 ms, the solid-liquid interface advances more slowly, which implies the eutectic growth velocity is non-constant at 230 K undercooling, showing the characteristics of slower growth at the beginning and end stages, the faster growth at the middle stage.

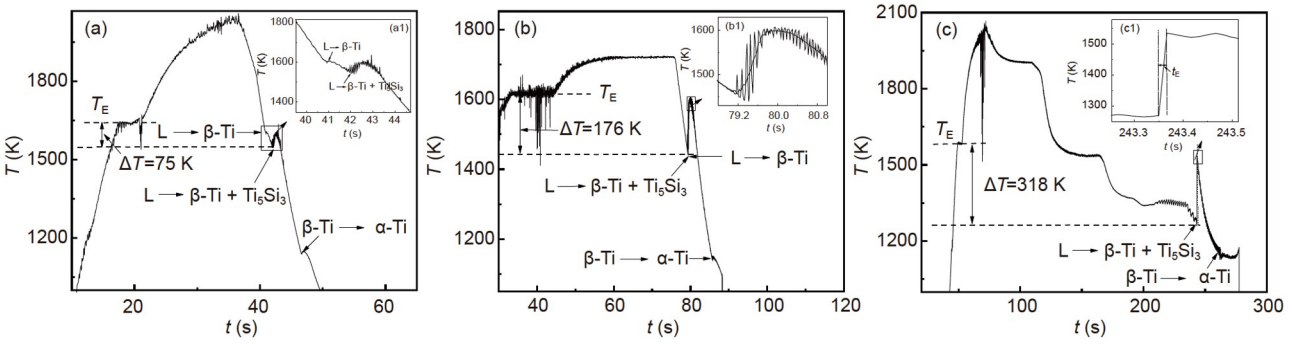

Figure 1 Heating and cooling curves of the electromagnetically levitated $Ti_{86.33}Si_{13.67}$ alloy. (a) ΔT = 75 K; (b) ΔT = 176 K; (c) ΔT = 318 K.

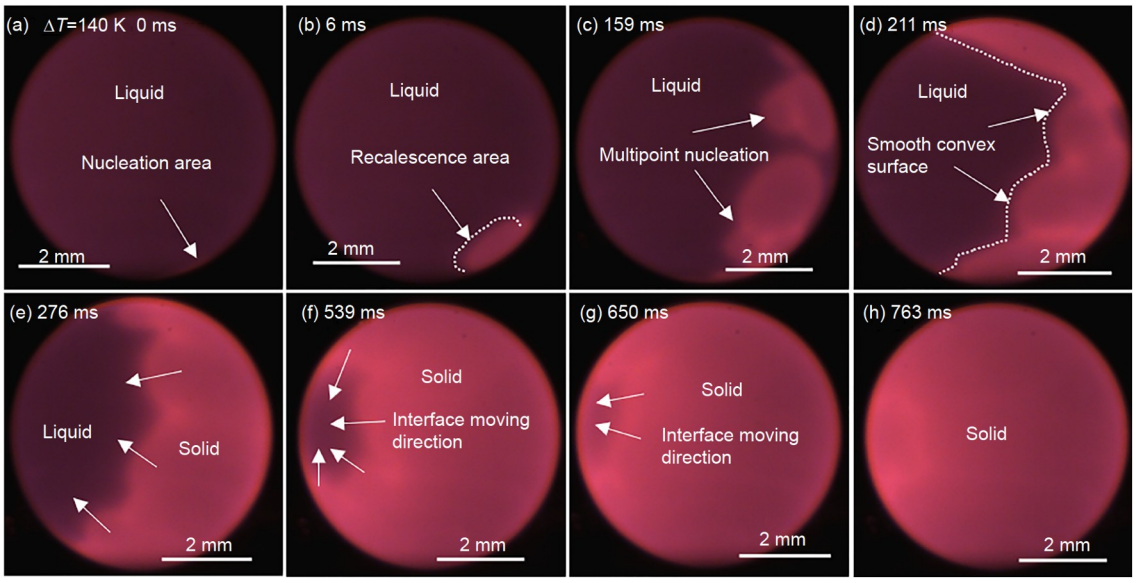

Figure 2 Interface of solid phase and undercooled liquid phase inside the electromagnetically levitated alloy at ΔT = 140 K. (a)–(h) Captured results at different time.

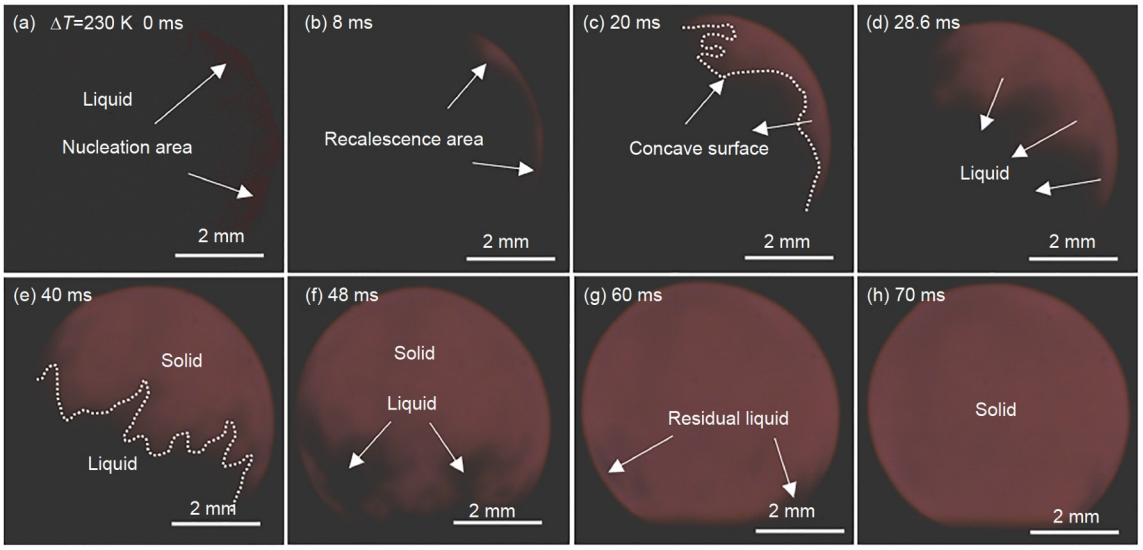

Figure 3 Interface of solid phase and undercooled liquid phase inside the electromagnetically levitated alloy at ΔT = 230 K. (a)–(h) Captured results at different time.

3.2 Phase characterization

Due to non-equilibrium solidification, phase composition is required to clarify the solidification path. During the solidification, there are envelopment reaction (β-Ti phase + Ti_5Si_3 phase → Ti_3Si phase) and eutectoid reaction (β-Ti phase → α-Ti phase + Ti_3Si phase) at the composition of $Ti_{86.33}Si_{13.67}$ alloy in the binary Ti-Si equilibrium phase diagram [32]. Based on the thermodynamic theory, Ti_3Si phase is most likely to be produced in the highly undercooled liquid phase. Therefore, both the XRD and TEM were used to analyses the solidified microstructure. As displayed in Figure 4, the XRD results indicate that the alloy consists of α-Ti, Ti_5Si_3 and Ti_3Si phases.

According to the thermodynamics, if Ti_3Si phase precipitates from the liquid phase, it is most likely to precipitate at higher undercoolings. Figure 5 shows the TEM results of rapidly solidified $Ti_{86.33}Si_{13.67}$ alloy under the electromagnetic levitation condition at 318 K undercooling. Both the diffraction spots in Figure 5 (c) and (d) show there is only one phase. The diffraction spots in Figure 5(c) indicate the matrix phase is α-Ti phase, while Figure 5(d) indicates the black rod-shaped phase is Ti_5Si_3 phase. The atomic percentage contents of Si in α-Ti phase and Ti_5Si_3 phase are (1.02 ±

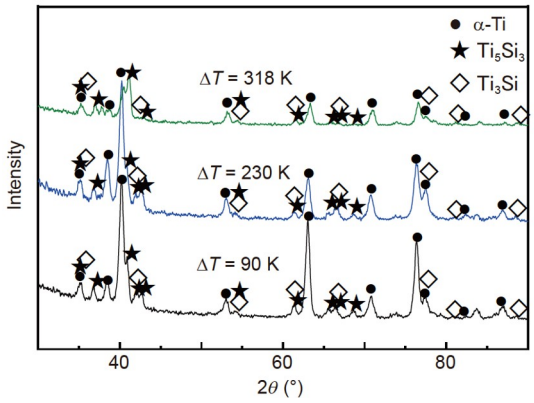

Figure 4 (Color online) Phase constitutions of solidified $Ti_{86.33}Si_{13.67}$ alloy at different undercoolings.

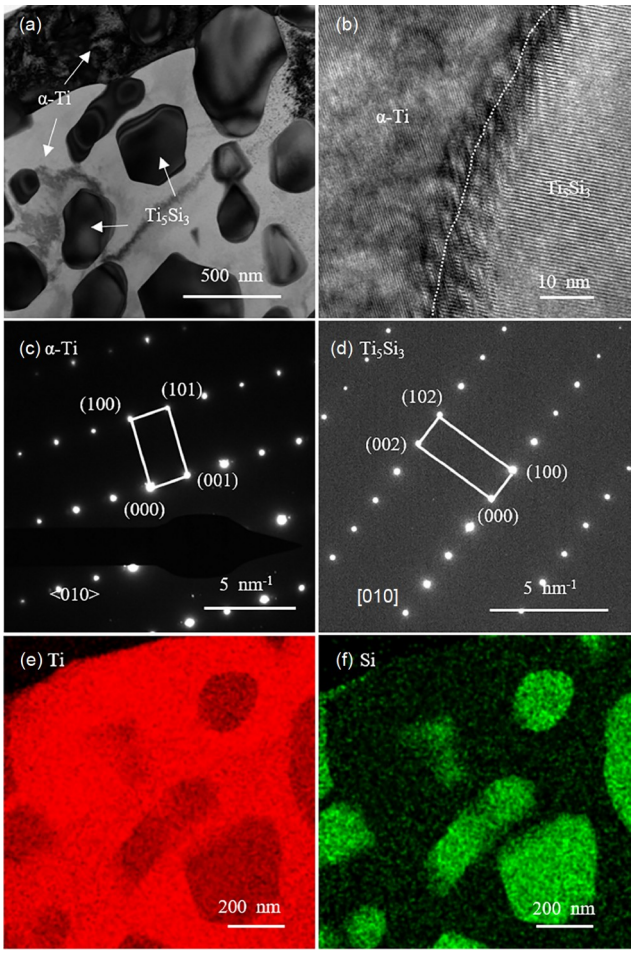

Figure 5 (Color online) TEM results of $Ti_{86.33}Si_{13.67}$ alloy solidified at 318 K undercooling. (a) Brightfield image of TEM sample; (b) the interface of α-Ti phase and Ti_5Si_3 phase; (c) selected area electron diffraction of α-Ti phase; (d) selected area electron diffraction of Ti_5Si_3 phase; (e) EDS mapping of Ti element; (f) EDS mapping of Si element.

0.476)at.% and (36.34 ± 2.72)at.%, respectively, which are consistent with the TEM results. The results of TEM and XRD indicate that the alloy solidified at the 318 K undercooling consists of α-Ti phase and Ti_5Si_3 phase, while the Ti_3Si phase is not found, which imply that the solid phase transition corresponding to the last exothermic peak on the cooling curves shown in Figure 1 is the transformation of β-Ti to α-Ti phase.

Meanwhile, the TEM results of rapidly solidified $Ti_{86.33}Si_{13.67}$ alloy through the drop tube experiment at D = 193 μm are shown in Figures 6 and 7. As shown in Figure 6(a)–(c), there are three phases in the microstructure which is composed of Ti and Si elements. Figure 6(d) shows a partial enlarged view of the Figure 6(a). It is shown that there are gray dotted phases in the black rod-shaped phase in addition to the dendritic phase. The selected diffraction spots of the dendritic phase shown in Figure 6(e) are confirmed to be the α-Ti phase. The selected diffraction spots of the black rod-shaped phase are shown in Figure 6(f), while the main diffraction spots are determined to be Ti_5Si_3 phase. As seen in Figure 7(d), the size of gray dotted phase is about 20 nm, and the crystal structure of the gray dotted phase cannot be directly determined by the diffraction spots in Figure 6(f). In order to get more information about the gray dotted phase shown in Figure 6(d), the high resolution TEM (HRTEM) and EDS analysis are conducted through a double Cs corrector transmission, as illustrated in Figure 7. The EDS results indicate that the content of Si in matrix α-Ti phase, Ti_5Si_3 phase and gray dotted phase in Figure 7(a) are (2.94 ± 0.71)at.%, (36.6 ± 6.02)at.%, and (27.52 ± 5.04)at.%, respectively. It should be noted that the matrix α-Ti phase here is the α-Ti phase in the eutectic rather than the dendritic α-Ti phase transformed from the primary dendritic β-Ti phase.

The HRTEM of the region composed of the Ti_5Si_3 phase and gray dotted phase is shown in Figure 7(d) where B region and the whole region defined as the A region are selected for fast Fourier transform (FFT). The FFT results of the B and A region are shown in Figure 7(e) and (f), respectively. Obviously, Figure 7(e) indicates there is only one phase to be confirmed as the Ti_5Si_3 phase. Figure 7(f) shows there are two sets of diffraction spots to be determined as the Ti_5Si_3 phase and Ti_3Si phase. Combined with the EDS results, it is confirmed that the gray dotted phase is Ti_3Si phase. It is worth noting that the crystal plane $(\bar{1}01)$ of the Ti_5Si_3 phase with the zone axis [121] and the crystal plane $(\bar{1}01)$ of the Ti_3Si phase with the zone axis $\langle 1\bar{1}1\rangle$ agree well. Moreover, it is interesting that the Ti_5Si_3 phase is embedded in matrix α-Ti phase while the Ti_3Si phase is also embedded in Ti_5Si_3 phase, while the Ti_3Si phase is neither found in the matrix α-Ti phase nor found in the dendritic α-Ti phase. The fact that the Ti_3Si phase appears inside the Ti_5Si_3 phase indicates the Ti_3Si phase does not match the way where the Ti_3Si phase is generated in the binary Ti-Si phase diagram. The Ti_3Si phase is most likely to be produced from the Ti_5Si_3 phase through a solid-state phase change. The reason for the solid-state transition may be that the Ti_5Si_3 phase formed by rapid solidification has high solid solution Ti atoms at high tem-

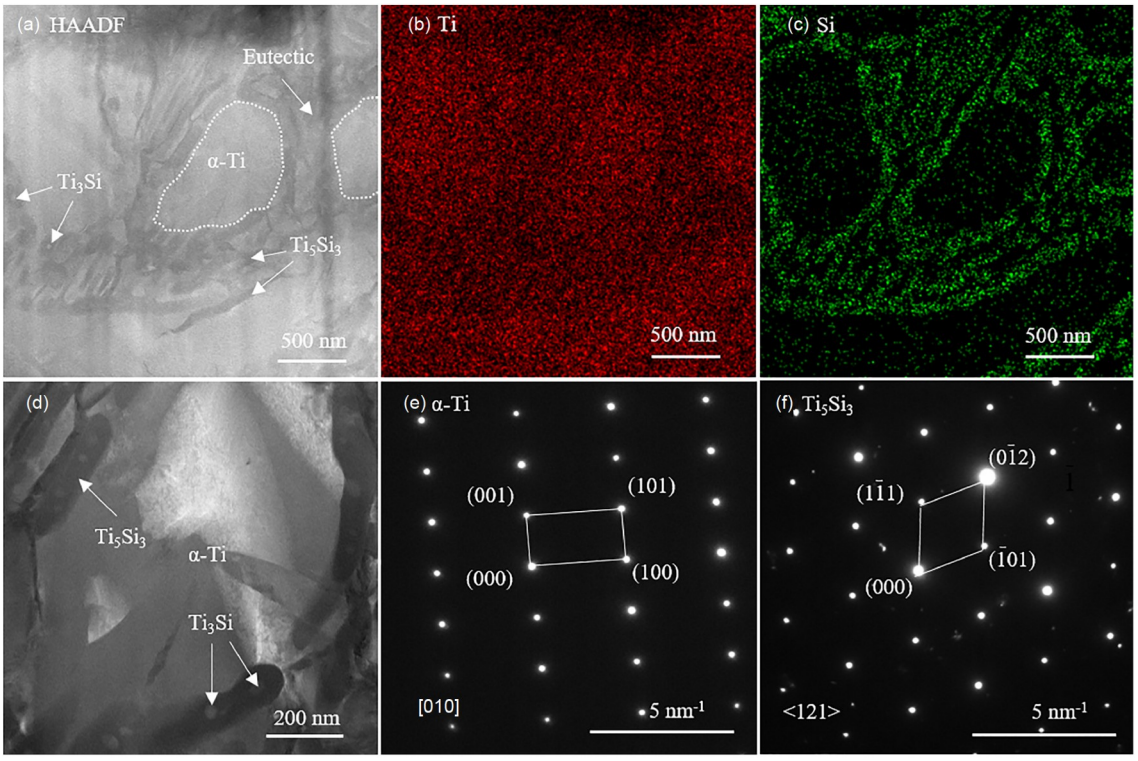

Figure 6 (Color online) TEM results of $Ti_{86.33}Si_{13.67}$ alloy solidified at D = 193 μm. (a) HAADF image of TEM sample; (b) EDS mapping of Ti element; (c) EDS mapping of Si element; (d) partial enlarged view of (a); (e) selected area electron diffraction of α-Ti phase; (f) selected area electron diffraction of Ti_5Si_3 phase.

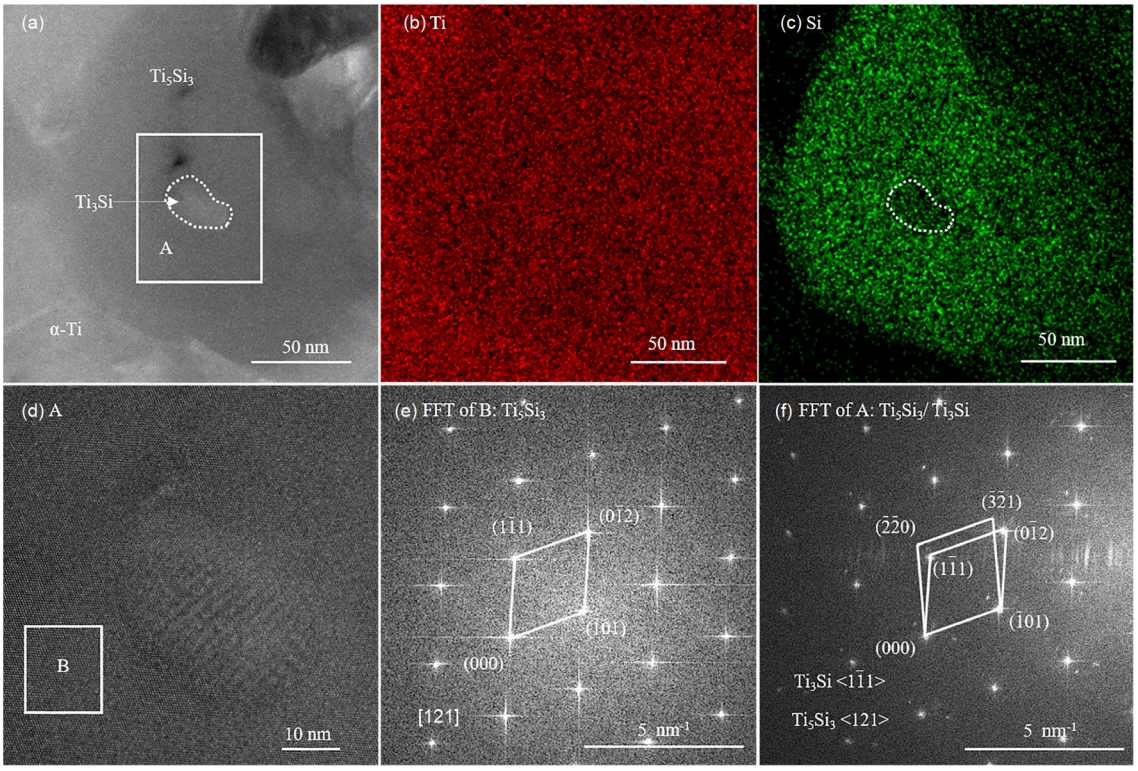

Figure 7 (Color online) HRTEM and EDS analyses of the gray dotted phase in the Ti_5Si_3 phase. (a) HAADF image of a selected region; (b) EDS mapping of Ti element; (c) EDS mapping of Ti element; (d) HRTEM of the region of Ti_5Si_3 phase and Ti_3Si phase; (e) FFT result of B region shown in (d); (f) FFT result of A region shown in (d).

peratures. As the temperature decreases, the high solid solution Ti atoms combine with Si atoms from the parent phase to nucleate and grow into Ti_3Si phase.

3.3 Eutectic growth kinetics

Combined the *in-situ* cooling curves with high-speed camera, the eutectic growth velocities of the undercooled $Ti_{86.33}Si_{13.67}$ alloy are obtained at different undercoolings as shown in Figure 8.

The average velocity v_{ME} of the eutectic reaction is expressed as the alloy diameter D to the whole eutectic reaction time t. The v_{ME} can be fitted as an exponential increase relationship with the increasing undercooling, as is shown in Figure 8. The fitting expression about the average eutectic reaction velocity can be expressed as

$$v_{ME} = 11370 \times \exp\left(-\frac{4.72\times10^8}{\Delta T^2 T}\right), \quad (1)$$

where T is the alloy temperature. It is generally believed that the growth velocity of dendrites increases with the increasing undercooling. Although the relationship between the average eutectic reaction velocity and the undercooling can be fitted by eq. (1), it is worth noting that the average reaction velocity has almost no change when $\Delta T < 200$ K. A reasonable explanation needs to be given to this phenomenon. Considering the alloys are undercooled and solidified in a changing external electromagnetic field, the effect of the external electromagnetic field on the alloy melt could not be ignored. It is conceivable that the most direct effect caused by the externally changing electromagnetic field is the electromagnetic stirring effect (EMSE) which accelerates the internal flow of liquid metal. More importantly, EMSE promotes the uniform distribution of the solute inside the undercooled liquid. Compared with the low solid solution phase, which is very beneficial for the formation of high solid solution phase. A finite element method (FEM) is used to simulate the flow field, the calculation formulars can refer to the ref. [33], and the results are shown in Figure 9. The physical parameters of the liquid $Ti_{86.33}Si_{13.67}$ alloy are listed in Table 1 [34,35], which are estimated by the linear superposition of pure Ti and Si elements.

With the increase of undercooling, the internal melt flow velocity decreases. This is mainly due to the increase of liquid viscosity at the macro level, which is manifested as an increase in the interaction among atoms. Though the liquid alloy is undercooled to 350 K, there is still a certain EMSE inside the alloy. At low and moderate undercooling, the eutectic reaction velocity has a hardly increase tendency with the increase of undercooling, which can be explained by the decrease of electromagnetic stirring effect. The increase trend of the eutectic reaction velocity weakens with the weakening of the EMSE, indicating that EMSE may play a key role in accelerating the eutectic reaction in this process.

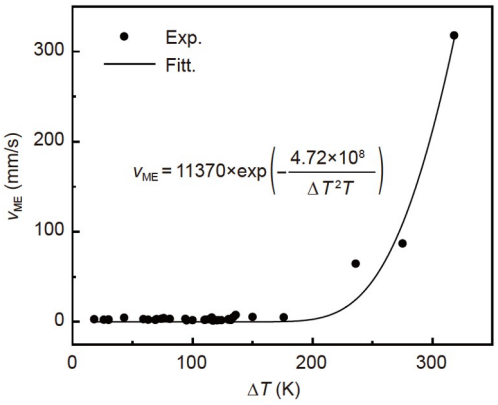

Figure 8 Average eutectic growth velocity of electromagnetically levitated $Ti_{86.33}Si_{13.67}$ alloy at different undercoolings.

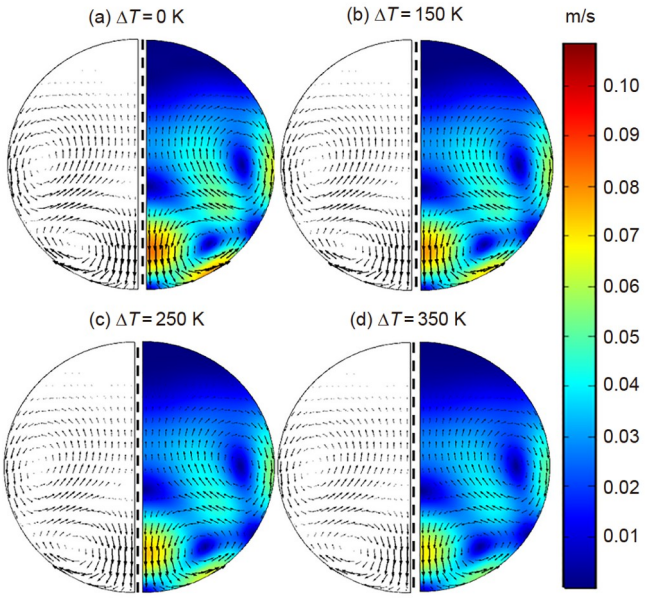

Figure 9 Internal flow velocity within electromagnetically levitated $Ti_{86.33}Si_{13.67}$ alloy melt at different undercoolings. (a) ΔT = 0 K; (b) ΔT = 150 K; (c) ΔT = 250 K; (d) ΔT = 350 K. The diameters of the alloy melts are set as 6 mm at the same place, and the left and right semicircles denote streamline field and velocity field, respectively.

However, as the undercooling increases further, the eutectic reaction velocity increases exponentially though there is a certain EMSE in liquid metal, indicating the changes in the intrinsic properties of liquid metal caused by high undercooling have played a major role. Setting E as the critical nucleation work of solid phase precipitated from the undercooled liquid phase [36]:

$$E \propto \frac{1}{\Delta T^2}, \quad (2)$$

substituting formula (2) into eq. (1):

$$v_{ME} = a_1 \times \left[\exp\left(-\frac{E}{RT}\right)\right]^{b_1}, \quad (3)$$

where a_1 and b_1 are the constants, and R the gas constant. According to the empirical relationship between chemical

reaction constant K and temperature [37]:

$$K = Z \times \exp[-E_a / RT], \quad (4)$$

where Z is a constant, and E_a the activation energy in a chemical reaction. The larger the K value, the faster the chemical reaction rate. Comparing eq. (4) with eq. (3), the growth velocity of the eutectic has a strong positive correlation with the chemical reaction constant, indicating that the eutectic growth can be explained from a perspective of chemical reaction.

3.4 Microstructure evolution

The microstructures solidified at 63, 90, and 176 K undercoolings are shown in Figure 10. For the convenience of expression, the α-Ti phase transformed from the primary dendritic β-Ti phase which primarily precipitates from the undercooled liquid phase and exists at the high temperature is called as the dendritic α-Ti phase, and the α-Ti phase in the eutectic is called as the matrix α-Ti phase. The figure in the right column is a partial enlarged view of the figure in the left column. It can be seen from Figure 10(a1) and (a2) that the microstructure consists of the dendritic α-Ti phase and eutectic at the 63 K undercooling, and the content of the dendritic α-Ti phase is obviously small, which shows that the first small exothermic peak on the cooling curve shown in Figure 1(a) is the transformation of L phase into β-Ti phase, and the second large exothermic peak is the transformation of L phase to eutectic phase. With the undercooling in-

Table 1 Physical parameters of the liquid $Ti_{86.33}Si_{13.67}$ alloy used for calculation [33,34]

Physical parameter	Undercooling ΔT (K)			
	0	150	250	350
Density ρ (g/cm^3)	3.742	3.779	3.804	3.828
Viscosity η (mPa s)	4.007	4.912	5.768	6.948
Electrical conductivity σ, 10^6 (S/m)	0.691	0.753	0.801	0.8562

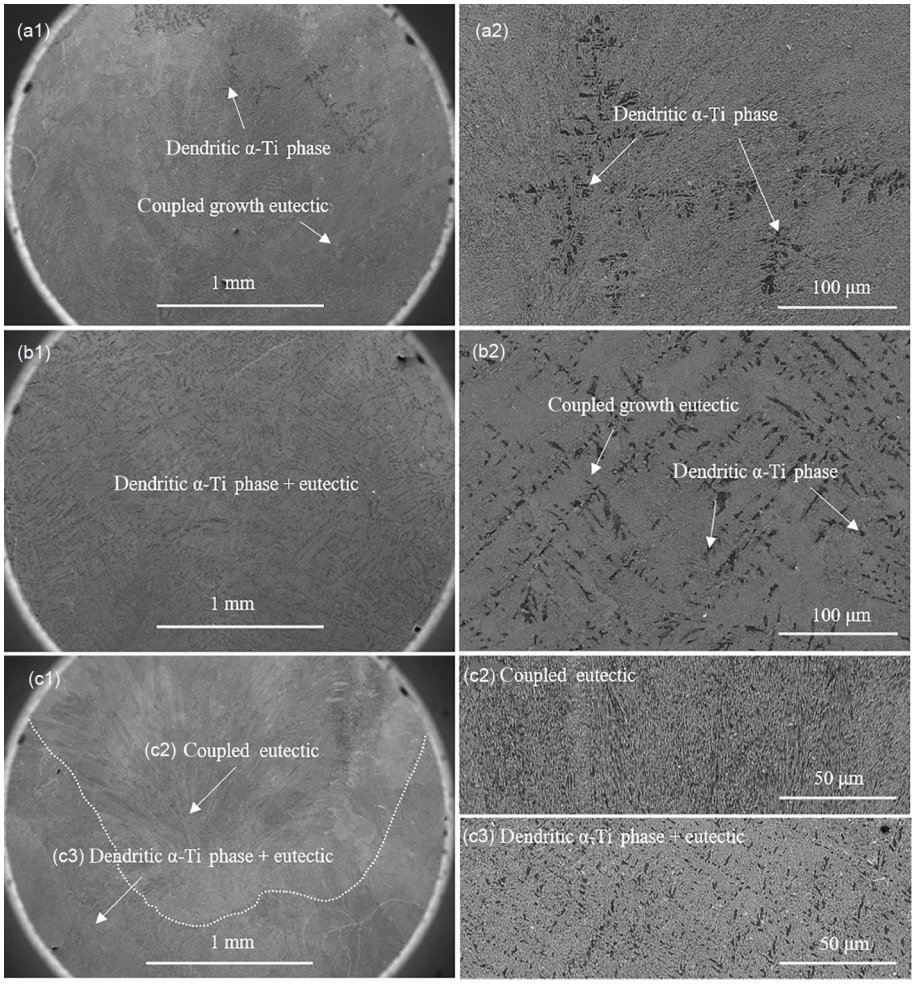

Figure 10 Microstructure of solidified alloy at different undercoolings. (a1), (a2) ΔT = 63 K; (b1), (b2) ΔT = 90 K; (c1)–(c3) ΔT = 176 K.

creasing to 90 K, it is found the solidified microstructure is composed of the dendritic α-Ti phase and eutectic, and the difference with the microstructure at the 63 K undercooling is that the α-Ti phase is dispersed throughout the sample, as shown in Figure 10(b1) and (b2). However, once the undercooling arrives at the 176 K, the microstructure is divided into two parts where one part is composed of the dendritic α-Ti phase and eutectic phase, and the other part is composed of eutectic phase which is shown in Figure 10(c1)–(c3). Synthesizing the changes from the microstructure solidified at 63 K undercooling to that at 176 K undercooling, the content of the dendritic α-Ti phase has a process of first increasing and then decreasing when the undercooling increases from 63 to 176 K. What needs to be further explored is how the microstructure will change as the undercooling increases further.

Since the optical microscope mode can see the difference in microstructure solidified at the 230, 273, and 318 K undercooling, several optical metallographic photos are used, which is shown in Figure 11. Firstly, eutectic reaction velocity at the middle stage is the fastest, and eutectic growth velocities at the beginning and last stages are relatively slow, which is also confirmed in Figure 3. The microstructure in Figure 11(a1)–(a3) further reflects the eutectic reaction process displayed in Figure 3.

As is shown in Figure 11(a1)–(a3), the figures in second column are partial enlarged views of the figures in the first column, while the figures in third column are partial enlarged views of the figures in the second column. The cluster-like microstructure mainly corresponds to the middle stage of eutectic reaction, i.e., the microstructure in the fast-grow area, while the microstructure between the cluster-like microstructure mainly corresponds to the last stage of growth. Whether it is the cluster-like eutectic microstructure or the microstructure between the cluster-like eutectic microstructure, the dendritic α-Ti phase has disappeared in those microstructures. With the undercooling increasing to 273 K, as displayed in Figures 10(b1)–(b3) and 11(b1)–(b3), the microstructure generated through the fast grow almost occupies the whole alloy compared with that on the 230 K condition. The slow-grow areas are so small that they are almost invisible, and the morphology of the microstructure in the slow growth area is very similar to the microstructure in the fast grow area. It is noting that the microstructure is composed of the irregular eutectic under the 273 K undercooling condition, and the size of the irregular eutectic is

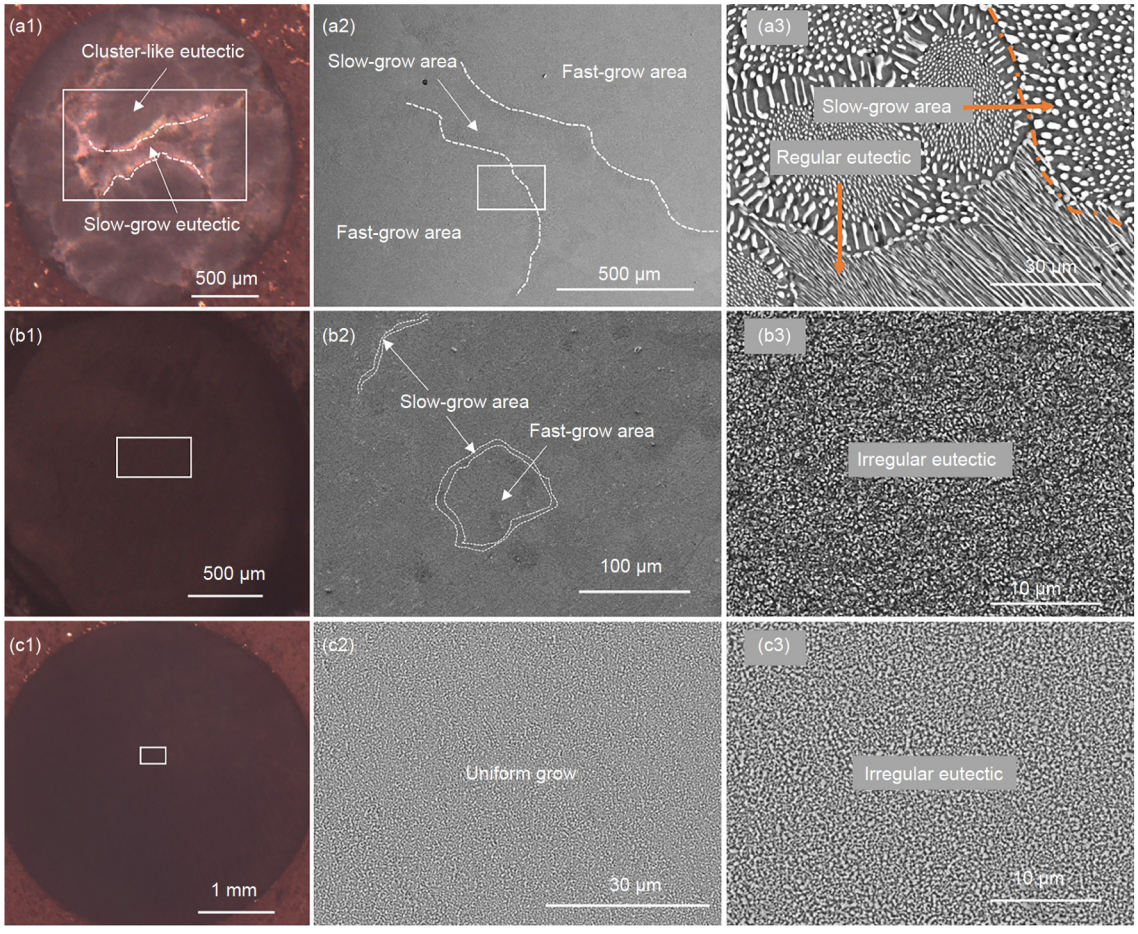

Figure 11 Microstructure of solidified alloy at high undercoolings. (a1)–(a3) ΔT = 230 K; (b1)–(b3) ΔT = 273 K; (c1)–(c3) ΔT = 318 K.

greatly refined. With the undercooling increasing to 318 K, the microstructure is composed of uniformly irregular eutectic, as shown in Figure 11(c1)–(c3). It can also be seen from the cooling curve shown in Figure 1(c) that the entire eutectic reaction process consists of a uniform recalescence process.

Analyzing the whole solidification process, it can be found that the microstructure is composed of dendritic α-Ti phase and eutectic when the undercooling is lower than 176 K. The microstructure is only composed of eutectic when the undercooling exceeds 230 K while the microstructure consists of irregular eutectic when undercooling is higher than 273 K. However, even at the 90 K undercooling where there is a large amount of dendritic α-Ti phase, the volume fraction of the dendritic α-Ti phase in the entire phase that composes the microstructure is still very small. Moreover, the solid solubility S of Si in the dendritic α-Ti phase is shown in Figure 12. It can be seen that the solid solubility of Si in the dendritic α-Ti phase fluctuates around the average value at five different undercoolings. However, at 130 K undercooling, there are more dendritic α-Ti phase where the solid solubility of Si is slightly larger than that at the other four undercoolings.

As shown in Figure 13, the microstructures of solidified droplets with different diameters D are obtained in the drop tube experiments. The figures in the first column reflect the profile of the solidified alloy, and the figures in second column are partial enlarged views of the first column figures. Microstructures consisting of a large amount of dendritic α-Ti phase and eutectic phase are found in a wide range of D from 69 to 725 μm. As seen in Figure 13, regardless of the particle size, the dendritic α-Ti phase is surrounded by one phase that is the Ti_5Si_3 phase, which is convinced from the analysis in Figure 6. Compared with the content of the dendritic α-Ti phase on the electromagnetic levitation condition shown in Figure 10, the content of the dendritic α-Ti phase has been significantly improved through the drop tube experiment. Moreover, as the particle diameter decreases, the content of the dendritic α-Ti phase obviously increases.

In order to characterize the cooling rate of the alloy droplet in the drop tube experiments, the calculated equation is expressed as

$$R_c = \frac{6}{C_P \rho_L D}(\varepsilon\sigma(T^4 - T_a^4) + h(T - T_a)), \quad (5)$$

where ρ_L is the liquid alloy density, C_P the heat capacity of liquid alloy, ε the surface emissivity, σ_s the Stefan-Boltzmann constant, T_a the ambient temperature and h the heat transfer coefficient whose calculation formula can be seen in refs. [38,39]. The physical parameters used for calculating the cooling rate of the liquid $Ti_{86.33}Si_{13.67}$ alloy are listed in Table 2 [40], and the parameters of the liquid alloy are also estimated by the linear superposition of pure Ti and Si elements.

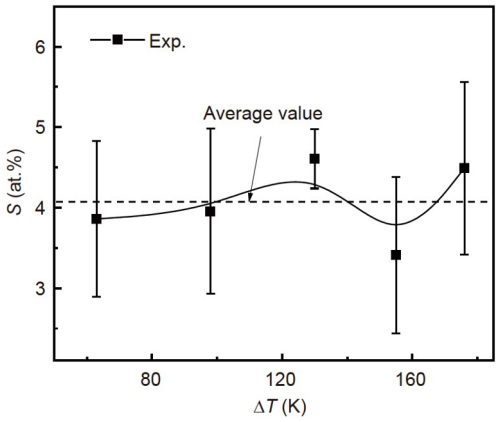

Figure 12 The solubility S of Si in the dendritic α-Ti phase.

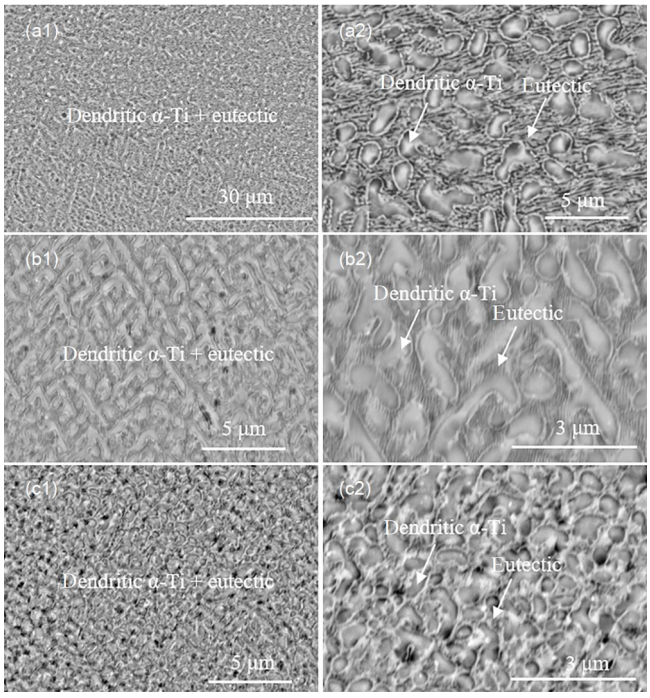

Figure 13 Microstructure of solidified alloy with different diameter D under drop tube conditions. (a1), (a2) D = 725 μm; (b1), (b2) D = 128 μm; (c1), (c2) D = 69 μm.

The cooling rate of the liquid alloy under the electromagnetic levitation condition is usually less than 1.0×10^2 K/s, and that is large than 3.0×10^3 K/s when the diameter of the alloy is smaller than 700 μm, and the cooling rate is as high as 2.6×10^5 K/s when the alloy droplet diameter is 70 μm. The cooling rates of liquid alloys of different diameters are displayed in Figure 14(a) where it can be seen the cooling rate of the liquid alloy increases as a power function with the decrease of diameter.

As is shown in Figures 10 and 11, increasing the undercooling cannot increase the content of the dendritic α-Ti phase. On the contrary, it will reduce the content of the

Table 2 Physical parameters of the liquid $Ti_{86.33}Si_{13.67}$ alloy used for calculation [40]

Physical parameters	Value
Liquidus temperature T_E (K)	1618
Density ρ_L (g/cm^3)	3.742×10^{-4}–2.467×10^{-4} $(T-T_E)$
Surface emissivity ε	0.29
Specific heat of liquid C_P (J kg^{-1} K^{-1})	752
Specific heat of mixed gas C_{PM} (J kg^{-1} K^{-1})	3324
Stefan-Boltzmann constant σ_S (10^{-8} W m^{-2} K^{-4})	5.67
Ambient temperature T_a (K)	293
Relative speed of droplet liquid V_0 (m/s)	2

dendritic α-Ti phase. Therefore, combining the results of Figures 10, 11, and 13, in addition to the appropriate undercooling, the drastically increased cooling rate is the main reason for obtaining more dendritic α-Ti phase. Since the volume of the phase in the three-dimensional space cannot be accurately known, the ratio f of the area occupied by the dendritic α-Ti on a cross-section is used as a parameter to characterize the content of dendritic α-Ti, and the results are shown in Figure 14(c). In order to further study the effect of the increased cooling rate on the dendritic α-Ti phase, the solid solubility S of Si in the dendritic α-Ti phase are analyzed for the solidified alloys prepared through the electromagnetic levitation and drop tube methods, and the result is displayed in Figures 12 and 14(b), respectively. As seen in the Figure 12, the average value of the S at different undercoolings is 4.06, and the S values under different undercoolings fluctuate up and down the average value under the electromagnetic levitation condition. However, the S increases dramatically with the decreasing D in the drop tube experiment, and the smallest S value shown in Figure 14(b) in the drop tube experiment is larger than the S value in Figure 12 under electromagnetic levitation condition. Therefore, the increase of S is positively correlated with the increased content of the dendritic α-Ti phase, which enriches the connotation of dendrite growth and microstructure controlling. From the views of the physical reaction and chemical reaction, it is easier to form a transition state of a disordered solid solution with high solubility in an undercooled liquid, because the energy required to form such a disordered solid solution is lower and the resistance is lower. Moreover, the EMSE is conducive to maintaining a uniform distribution of solutes in the undercooled liquid, creating an environment conducive to form solid solutions with high solubility. With the help of the large cooling rate and appropriate undercooling as well as the EMSE, a dendritic α-Ti phase with high solubility was obtained at the room temperature, which is proven by the solidification results through the electromagnetic levitation and drop tube extraordinary experiments.

4 Conclusions

The rapid solidification of the liquid eutectic $Ti_{86.33}Si_{13.67}$ alloy was accomplished with the help of electromagnetic levitation and drop tube techniques, and the maximum undercooling achieved by electromagnetic levitation method was 318 K ($0.2T_E$). When the undercooling is smaller than 140 K, the liquid-solid interface is smooth, and the eutectic growth is controlled by solute diffusion. When the undercooling arrives at 230 K, the liquid-solid interface is irregular, and the eutectic growth is controlled by solute diffusion and thermal diffusion. The eutectic growth velocity increases as a power function of undercooling. The electromagnetic stirring effect weakens the undercooling, and plays an important role in accelerating the eutectic reaction velocity at low and moderate undercoolings.

In the case of 63 to 176 K undercoolings, primary dendritic β-Ti phase appears within the undercooled liquid alloy. When the undercoolings increase up to 230 K, there is no dendritic α-Ti phase in the microstructure which is completely composed of eutectic. As the undercoolings are higher than 273 K, the microstructure consists of irregular eutectic which is distributed uniformly. The alloys solidified in the electromagnetic levitation experiment are composed of α-Ti phase and Ti_5Si_3 phase, while the Ti_3Si phase is found inside the Ti_5Si_3 phase in a solidified alloy with 193 μm

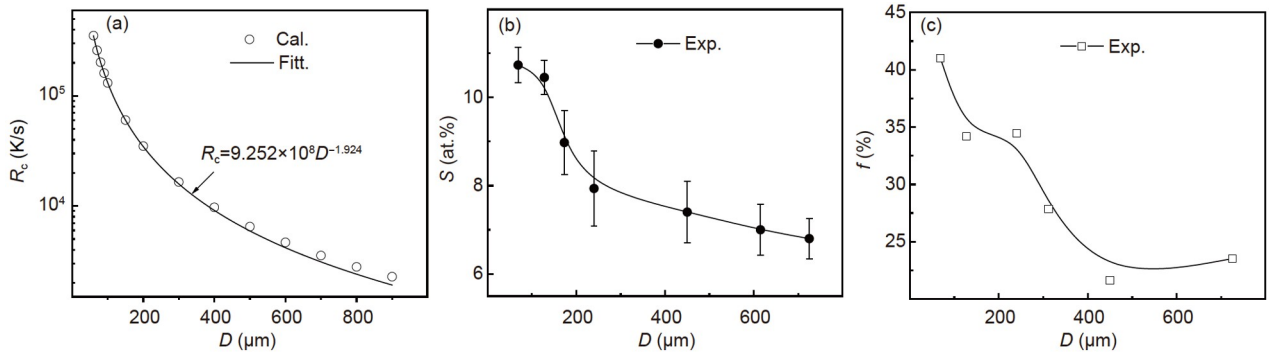

Figure 14 The cooling rate of the alloy, the S and the content of dendritic α-Ti phase under the drop tube condition. (a) The cooling rate; (b) the solid solubility S in the dendritic α-Ti phase; (c) ratio of the area occupied by the dendritic α-Ti on a cross-section.

diameter in the drop tube experiment.

Microstructures consisting of a large amount of dendritic α-Ti phase and eutectic phase are found in a wide range of D from 69 to 725 μm in the drop tube experiment. As D decreases from 725 to 69 μm, the solid solubility of Si in the dendritic α-Ti phase increases dramatically from 6.8% to 10.73%, and the ratio of the area occupied by the dendritic α-Ti on a cross-section of solidified alloy increases obviously from 23.52% to 41.02%. The main reason for the increase of Si solid solubility in the dendritic α-Ti phase and the increase of dendritic α-Ti phase in the solidified alloy are the combined effects of the appropriate undercooling and large cooling rate.

This work was supported by the National Key R&D Program of China (Grant No. 2018YFB2001800), and the National Natural Science Foundation of China (Grant Nos. 51734008, 51771154, and 52088101). We are grateful to Miss. Wang Xiaojuan, Mr. Zuo Dongdong and Dr. Cai Xiao for their help of experiment. We are especially grateful to Prof. Wei Bingbo for the experimental support.

1 Liu G, Zhang G J, Jiang F, et al. Nanostructured high-strength molybdenum alloys with unprecedented tensile ductility. Nat Mater, 2013, 12: 344–350
2 Löser W, Leonhardt M, Lindenkreuz H G, et al. Phase selection in undercooled binary peritectic alloy melts. Mater Sci Eng-A, 2004, 375-377: 534–539
3 Wu Y H, Chang J, Wang W L, et al. Metastable coupled-growth kinetics between primary and peritectic phases of undercooled hypoperitectic $Fe_{54.5}Ti_{45.5}$ alloy. Appl Phys Lett, 2016, 109: 154101
4 Wang Q, Zhai B, Wang H P, et al. Atomic structure of liquid refractory Nb_5Si_3 intermetallic compound alloy based upon deep neural network potential. J Appl Phys, 2021, 130: 185103
5 Zhang P C, Hu Y J, Chang J, et al. Microscopic hardness and dynamic mechanical analysis of rapidly solidified Fe-based amorphous alloys. J Alloys Compd, 2021, 861: 157957
6 Yang T, Han Y, Li J. Manipulating silver dendritic structures via diffusion and reaction. Chem Eng Sci, 2015, 138: 457–464
7 Luo Z C, Wang H P. Primary dendrite growth kinetics and rapid solidification mechanism of highly undercooled Ti-Al alloys. J Mater Sci Tech, 2020, 40: 47–53
8 Sun G, Xu J, Harrowell P. The mechanism of the ultrafast crystal growth of pure metals from their melts. Nat Mater, 2018, 17: 881–886
9 Vekilov P G. Nucleation. Cryst Growth Des, 2010, 10: 5007–5019
10 Wang H P, Lü P, Cai X, et al. Rapid solidification kinetics and mechanical property characteristics of Ni-Zr eutectic alloys processed under electromagnetic levitation state. Mater Sci Eng-A, 2020, 772: 138660
11 Trivedi R, Magnin P, Kurz W. Theory of eutectic growth under rapid solidification conditions. Acta Metall, 1987, 35: 971–980
12 Lipton J, Kurz W, Trivedi R. Rapid dendrite growth in undercooled alloys. Acta Metall, 1987, 35: 957–964
13 Hu L, Yang S J, Wang L, et al. Dendrite growth kinetics of β-Zr phase within highly undercooled liquid Zr-Si hypoeutectic alloys under electrostatic levitation condition. Appl Phys Lett, 2017, 110: 164101
14 Liu L, Li J F, Zhou Y H. Solidification interface morphology pattern in the undercooled Co-24.0at.% Sn eutectic melt. Acta Mater, 2011, 59: 5558–5567
15 Lee B, Paek E, Mitlin D, et al. Sodium metal anodes: Emerging solutions to dendrite growth. Chem Rev, 2019, 119: 5416–5460
16 Sun C T, Xue D F. Chemical bonding in micro-pulling down process: High throughput single crystal growth. Sci China Tech Sci, 2018, 61: 1776–1778
17 Jeon S, Heo T, Hwang S Y, et al. Reversible disorder-order transitions in atomic crystal nucleation. Science, 2021, 371: 498–503
18 Lutsko J F, Nicolis G. Theoretical evidence for a dense fluid precursor to crystallization. Phys Rev Lett, 2006, 96: 046102
19 Xu M, Ge X, Yao W, et al. Atomic distance tuning effect for nucleation in liquid iron. Metall Mat Trans A, 2018, 49: 4419–4423
20 Mullis A M, Clopet C R. On the origin of anomalous eutectic growth from undercooled melts: Why re-melting is not a plausible explanation. Acta Mater, 2018, 145: 186–195
21 Luo S B, Wang W L, Xia Z C, et al. Theoretical prediction and experimental observation for microstructural evolution of undercooled nickel-titanium eutectic type alloys. J Alloys Compd, 2017, 692: 265–273
22 Zhao J F, Wang H P, Wei B. A new thermodynamically stable Nb_2Ni intermetallic compound phase revealed by peritectoid transition within binary Nb-Ni alloy system. J Mater Sci Tech, 2022, 100: 246–253
23 Zhang X, Chen Y, Hu J. Recent advances in the development of aerospace materials. Prog Aerospace Sci, 2018, 97: 22–34
24 Chen G, Peng Y, Zheng G, et al. Polysynthetic twinned TiAl single crystals for high-temperature applications. Nat Mater, 2016, 15: 876–881
25 Shuleshova O, Holland-Moritz D, Löser W, et al. *In situ* observations of solidification processes in γ-TiAl alloys by synchrotron radiation. Acta Mater, 2010, 58: 2408–2418
26 Liu W, Yan N, Wang H P. Dendritic morphology evolution and microhardness enhancement of rapidly solidified Ni-based superalloys. Sci China Tech Sci, 2019, 62: 1976–1986
27 Liu T, Luo L S, Zhang D H, et al. Comparison of microstructures and mechanical properties of as-cast and directionally solidified Ti-47Al-1W-0.5Si alloy. J Alloys Compd, 2016, 682: 663–671
28 Wang Q, Wang H P, Geng D L, et al. Experimental determination of the Ni-Ni_5Zr eutectic point for binary Ni-Zr alloy phase diagram. Appl Phys A, 2020, 126: 375
29 Matson D M, Xiao X, Rodriguez J E, et al. Use of thermophysical properties to select and control convection during rapid solidification of steel alloys using electromagnetic levitation on the space station. JOM, 2017, 69: 1311–1318
30 Luo Z C, Wang H P. Combined effects of high undercooling and large cooling rate on the microstructure evolution and hardening mechanism of rapidly solidified Ti-Al alloys. Metall Mater Trans A, 2020, 51: 1242–1253
31 Wu Y H, Chang J, Wang W L, et al. A triple comparative study of primary dendrite growth and peritectic solidification mechanism for undercooled liquid $Fe_{59}Ti_{41}$ alloy. Acta Mater, 2017, 129: 366–377
32 Franke P, Seifert H J. Ternary Steel Systems: Phase Diagrams and Phase Transition Data. Springer, 2012
33 Lin M J, Chang J, Wu Y H, et al. Fluid convection and solidification mechanisms of liquid $Fe_{50}Cu_{50}$ alloy under electromagnetic levitation condition. Acta Phys Sin, 2017, 66: 136401
34 Ishikawa T, Paradis P F, Okada J T, et al. Viscosity measurements of molten refractory metals using an electrostatic levitator. Meas Sci Technol, 2012, 23: 025305
35 Rhim W K, Ohsaka K. Thermophysical properties measurement of molten silicon by high-temperature electrostatic levitator: Density, volume expansion, specific heat capacity, emissivity, surface tension and viscosity. J Cryst Growth, 2000, 208: 313–321
36 Kurz W, Fisher D J. Fundamentals of Solidification. 4th ed. Beijing: Higher Education Press, 2010. 18–28
37 Kang L J, Piao F Y. General Chemistry. 4th ed. Beijing: Higher Education Press, 2005. 20–40
38 Li M X, Wang H P, Yan N, et al. Heat transfer of micro-droplet during free fall in drop tube. Sci China Tech Sci, 2018, 61: 1021–1030
39 Lee E S, Ahn S. Solidification progress and heat transfer analysis of gas-atomized alloy droplets during spray forming. Acta Metall Mater, 1994, 42: 3231–3243
40 Smithells C J. Metals Reference Book. 6th ed. London: Butterworth, 1984